Comprehensive comparison of pore-scale models for multiphase flow in porous media

Benzhong Zhao[a], Christopher W. MacMinn[b], Bauyrzhan K. Primkulov[c], Yu Chen[d], Albert J. Valocchi[d], Jianlin Zhao[e], Qinjun Kang[f], Kelsey Bruning[g], James E. McClure[h], Cass T. Miller[g], Abbas Fakhari[i], Diogo Bolster[i], Thomas Hiller[j], Martin Brinkmann[k], Luis Cueto-Felgueroso[l], Daniel A. Cogswell[m], Rahul Verma[n], Maša Prodanović[n], Julien Maes[o], Sebastian Geiger[o], Morten Vassvik[p], Alex Hansen[p], Enrico Segre[q], Ran Holtzman[r,s], Zhibing Yang[t], Chao Yuan[u], Bruno Chareyre[u], and Ruben Juanes[c,1]

[a]Department of Civil Engineering, McMaster University, Hamilton, ON L8S 4L7, Canada; [b]Department of Engineering Science, University of Oxford, Oxford OX1 3PJ, United Kingdom; [c]Department of Civil and Environmental Engineering, Massachusetts Institute of Technology, Cambridge, MA 02139; [d]Department of Civil and Environmental Engineering, University of Illinois at Urbana–Champaign, Urbana, IL 61801; [e]Department of Mechanical and Process Engineering, Swiss Federal Institute of Technology in Zürich, 8092 Zürich, Switzerland; [f]Earth and Environmental Sciences Division, Los Alamos National Laboratory, Los Alamos, NM 87545; [g]Department of Environmental Sciences and Engineering, University of North Carolina at Chapel Hill, Chapel Hill, NC 27516; [h]Advanced Research Computing, Virginia Polytechnic Institute & State University, Blacksburg, VA 24061; [i]Department of Civil and Environmental Engineering and Earth Sciences, University of Notre Dame, Notre Dame, IN 46556; [j]Leibniz Institute for Applied Geophysics, 30655 Hannover, Germany; [k]Department of Experimental Physics, Saarland University, 66123 Saarbrücken, Germany; [l]Department of Civil Engineering, Universidad Politécnica de Madrid, 28040 Madrid, Spain; [m]Aramco Research Center-Boston, Aramco Services Company, Cambridge, MA 02139; [n]Department of Petroleum and Geosystems Engineering, University of Texas at Austin, Austin, TX 78712; [o]Institute of Petroleum Engineering, Heriot-Watt University, Edinburgh EH14 4AS, United Kingdom; [p]Department of Physics, Norwegian University of Science and Technology, 7491 Trondheim, Norway; [q]Department of Physics Core Facilities, Weizmann Institute of Science, Rehovot 76100, Israel; [r]Faculty of Agriculture, Food and Environment, The Hebrew University of Jerusalem, Rehovot 7610001, Israel; [s]Faculty of Engineering, Environment and Computing, Coventry University, Coventry CV1 2JH, United Kingdom; [t]State Key Laboratory of Water Resources and Hydropower Engineering Science, Wuhan University, Wuhan 430072, China; and [u]Laboratoire 3SR, Université Grenoble Alpes, 38041 Grenoble, France

Multiphase flows in porous media are important in many natural and industrial processes. Pore-scale models for multiphase flows have seen rapid development in recent years and are becoming increasingly useful as predictive tools in both academic and industrial applications. However, quantitative comparisons between different pore-scale models, and between these models and experimental data, are lacking. Here, we perform an objective comparison of a variety of state-of-the-art pore-scale models, including lattice Boltzmann, stochastic rotation dynamics, volume-of-fluid, level-set, phase-field, and pore-network models. As the basis for this comparison, we use a dataset from recent microfluidic experiments with precisely controlled pore geometry and wettability conditions, which offers an unprecedented benchmarking opportunity. We compare the results of the 14 participating teams both qualitatively and quantitatively using several standard metrics, such as fractal dimension, finger width, and displacement efficiency. We find that no single method excels across all conditions and that thin films and corner flow present substantial modeling and computational challenges.

porous media | capillarity | wettability | pattern formation | simulation

Multiphase flows in porous media are central to a wide range of natural and industrial processes, including geologic CO_2 sequestration, enhanced oil recovery, and water infiltration into soil. Predictive modeling of these processes requires a clear understanding of the pore-scale mechanisms of fluid–fluid displacement. These pore-scale processes can be simulated using a variety of different approaches, including lattice/particle-based methods such as the lattice Boltzmann method, upscaled continuum methods such as phase-field models, and topological methods such as pore-network models (1). All of these models must confront a variety of fundamental challenges related to resolving the combined effects of capillarity, wetting, and viscous instability within a complex geometry, including thin films, moving contact lines, and the pinch off and merging of interfaces. These mechanisms combine to produce macroscopic displacement patterns that are strongly dependent on the relative affinity of the solid for the different fluids (i.e., wettability), the importance of viscous forces relative to capillary forces (i.e., capillary number), and the pore geometry. As a result, pore-scale modeling of multiphase flow in porous media, even for relatively simple

pore geometries, remains an open challenge and a very active area of research.

Historically, comparisons between pore-scale models and experimental data have been hampered by limitations on both fronts. The vast majority of existing experimental observations have been limited to macroscopic features and a narrow range of wettability conditions (strong drainage), and do not include a precise description of the associated pore geometry. In addition, most pore-scale models are very computationally expensive; only recently have these methods been able to simulate flow through a sufficiently large number of pores to reproduce macroscopic observables due to advances in both modeling methods

Significance

The simultaneous flow of multiple fluid phases through a porous solid occurs in many natural and industrial processes. Microscale physical mechanisms such as the relative affinity of the solid for the fluids (i.e., wettability), capillarity, and viscosity combine with pore geometry to produce a wide variety of macroscopic flow patterns. Pore-scale modeling is an essential tool to connect microscale mechanisms with macroscopic patterns, but quantitative comparisons between different models, and with experimental data, are lacking. Here, we perform an unprecedented comparison of state-of-the-art models from 14 leading groups with a recent experimental dataset. The results underscore the challenges of simulating multiphase flows through porous media, highlighting specific areas for further effort in what is already a flourishing field of research.
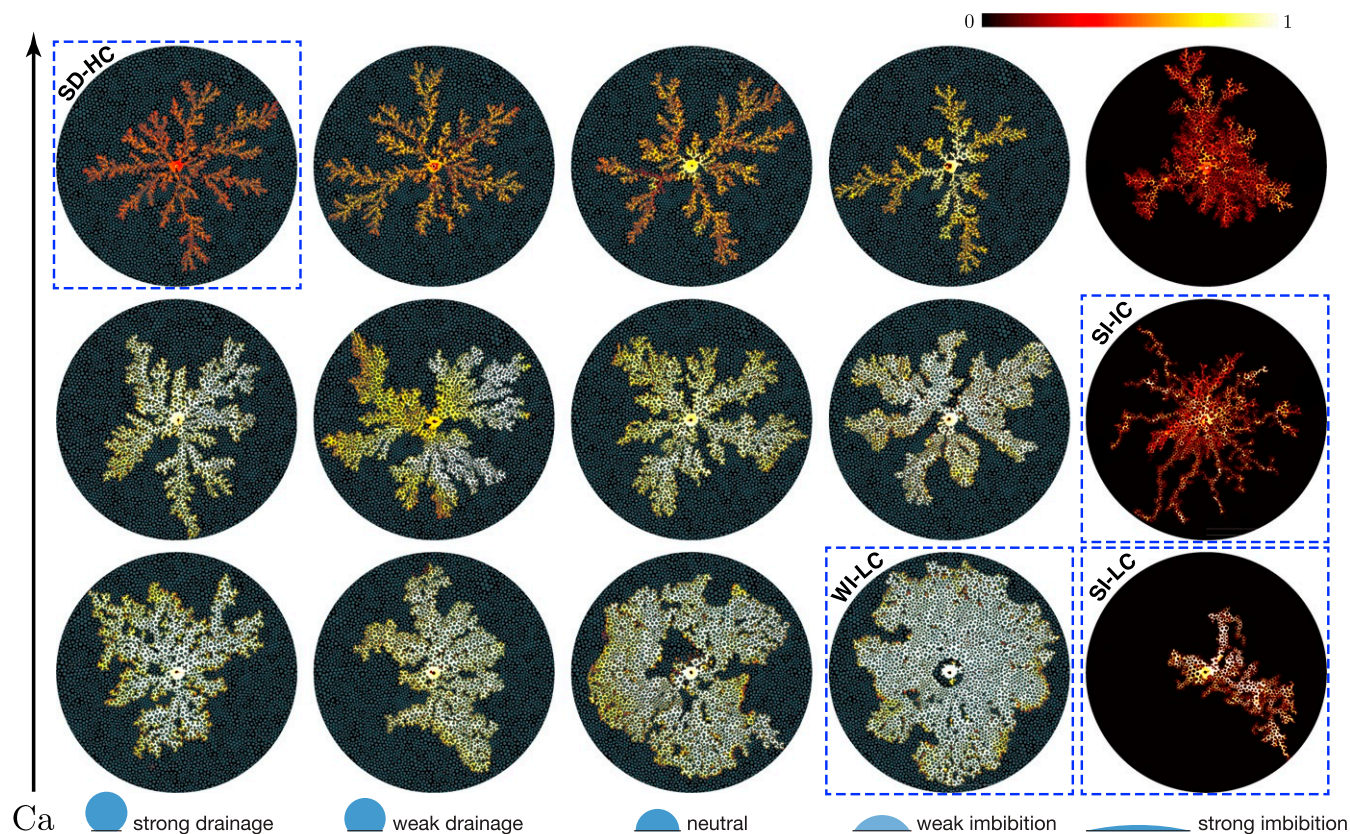
APPLIED PHYSICAL SCIENCES

Fig. 1. Experimental phase diagram showing the displacement pattern at breakthrough for different wettability conditions (*Left* to *Right*: $\theta = 150°$, $120°$, $90°$, $60°$, $7°$) and capillary numbers (*Bottom* to *Top*: Ca = 0.029, 0.29, 2.9). The colormap shows the gap-averaged saturation of the invading fluid. The four "priority cases" for the benchmark study are outlined in dashed blue: strong drainage at high Ca (SD-HC), weak imbibition at low Ca (WI-LC), strong imbibition at intermediate Ca (SI-IC), and strong imbibition at low Ca (SI-LC). Diagram is adapted from ref. 2.

and computing power. At the same time, modern experimental techniques now allow for high-resolution experimental observations and detailed characterization of pore geometry (1). One recent dataset, in particular, provides high-resolution observations across a wide range of wettabilities and capillary numbers in a well-defined and relatively simple pore geometry (2). These observations offer an unprecedented benchmarking opportunity for pore-scale models. The goal of this benchmark is to compare a wide variety of state-of-the-art pore-scale modeling approaches with experimental observations in terms of both pore-scale mechanisms and macroscopic displacement patterns.

Results

Dataset. The benchmark study is based on the experiments of Zhao *et al.* (2) (Fig. 1). In the experiments, water ($\eta_{\text{water}} = 0.99$ mPa·s) was injected into a viscous silicone oil ($\eta_{\text{oil}} = 340$ mPa·s) in quasi-2D microfluidic flow cells patterned with vertical posts. This is a strongly viscously unstable displacement with viscosity ratio $\mathcal{M} = \eta_{\text{oil}}/\eta_{\text{water}} \approx 340$. The large unfavorable viscosity ratio of the experimental dataset was motivated by several considerations: It allows for direct comparison with previous wettability-related experimental studies (3, 4), it helps to highlight the impact of wettability on viscous instabilities, and it is directly relevant to applications like waterflooding of heavy crude oil (5).

The importance of viscous forces relative to capillary forces in the experiments was characterized using the classical capillary number Ca = $\eta_{\text{oil}} v_{\text{inj}}/\gamma$, where $\gamma = 13 \pm 2$ mN/m is the interfacial tension between the fluids and $v_{\text{inj}} = Q/(bd)$ is the characteristic injection velocity as constrained by the gap thick-

ness $b = 100$ μm and the median pore-throat size $d = 300$ μm. The experiments were conducted at three distinct values of Ca spanning two orders of magnitude: Ca = 0.029 ("low Ca"), 0.29 ("intermediate Ca"), and 2.9 ("high Ca").[*] Note that these values of Ca provide a nominal macroscopic characterization of the flow, but the actual strength of viscous to capillary forces varies locally due pore-scale heterogeneity, preferential pathways, and the radial flow geometry. Note also that the lowest value of Ca considered here is still moderate relative to a truly quasi-static displacement. The wettability of the flow cell was characterized using the static advancing contact angle θ of water immersed in silicone oil. The experiments were conducted at five distinct values of θ spanning the full range of wettability conditions: $\theta = 150°$ ("strong drainage"), $120°$ ("weak drainage"), $90°$ ("neutral"), $60°$ ("weak imbibition"), and $7°$ ("strong imbibition"). The participating teams were given the exact geometry of the post pattern and, for each experimental condition, a series of data files describing the time evolution of the gap-averaged water saturation S at high spatial resolution. To allow for qualitative and quantitative comparisons between methods without imposing an excessive computational burden on participants, we identified four "priority cases" that best represent the diversity of patterns and physical mechanisms that emerge from fluid–fluid displacement under different Ca and wettability conditions: (*i*) strong drainage at high Ca (SD-HC), canonical viscous fingering pattern with incomplete pore-scale

---

[*]Note that the Ca values reported in ref. 2 are incorrect—they are too small by one order of magnitude.

displacement due to formation of trailing films of the defending fluid; (*ii*) weak imbibition at low Ca (WI-LC), compact displacement pattern due to cooperative pore filling; (*iii*) strong imbibition at intermediate Ca (SI-IC), thin-film flow of the invading fluid along the top and bottom walls, accompanied by a ramified fingering pattern formed by corner flow; and (*iv*) strong imbibition at low Ca (SI-LC), corner-flow–driven "chaining" of posts.

Participating Teams and Methods. A total of 14 teams contributed modeling results to the benchmark study (Table 1). Together, they applied many different pore-scale modeling methods (Table 1 and *SI Appendix*, Note 1). The methods can be categorized into three major classes: lattice/particle-based models, continuum models, and pore-network models. Lattice/particle-based models simulate the motion and interaction of a large number of microscopic particles that collectively give rise to macroscopic behavior satisfying the relevant continuum equations (e.g., Navier–Stokes). The fluid–fluid interface is captured implicitly as the boundary between the multicolored particles that represent the different fluid phases. These models include lattice Boltzmann (LB) methods (34) and stochastic rotation dynamics (SR) models (35). Continuum models solve macroscopic equa-

tions for fluid flow while tracking the interface implicitly via the evolution of an indicator variable. These models include volume-of-fluid (VF) methods (36), level-set (LS) methods (37), and phase-field (PF) models (38). Pore-network (PN) models simulate fluid flow through an idealized network of pores connected by throats (39). The macroscopic interface is represented explicitly as the boundary between invaded and noninvaded pores. It speaks to the physical complexity of this problem that only one of the contributions (VF1) attempted direct simulation of the Navier–Stokes (or Stokes) equations with evolving fluid–fluid interfaces. Note also that only LB1, LB3, and SR1 conducted truly 3D simulations.

Qualitative Performance Measures. The interplay between wettability and Ca generates a wide spectrum of 2D displacement patterns that range from ramified fingers to compact fronts (Fig. 1). Additional 3D information is provided by the local gap-averaged saturation of the invading fluid (Fig. 1). The displacement pattern and saturation distribution at the end of the simulation, when the invading fluid reaches the outer edge of the computational domain, serve as a good basis for qualitative and quantitative comparisons (e.g., Figs. 2 and 3 and *SI Appendix*).

Table 1. Summary of contributions

Label	Authors	Method	Dim.	Comp. dom., %	Res.	$\mathcal{M}$	Remarks	Refs.
LB1	Y.C. A.J.V.	Lattice Boltzmann	3	50, 80	14.3	5, 40, 100	Artificial precursor film in strong imbibition.	(6, 7)
LB2	J.Z. Q.K.	Lattice Boltzmann	2	100	20.2	340	Perturbation and recoloring operators generate interfacial tension and phase segregation, respectively.	(8, 9)
LB3	K.B. J.E.M. C.T.M.	Lattice Boltzmann	3	40	13	100	Increased domain thickness to 448 μm to better resolve film formation in the gap.	(10, 11)
LB4	A.F. D.B.	Lattice Boltzmann	2	100	∼100	340	LB equation based on the conservative phase-field method.	(12, 13)
SR1	T.H. M.B.	Stochastic rotation dynamics	3	60	∼300	1–5	Limited resolution in the gap, leading to unrepresentative saturation.	(14, 15)
PF1	L.C.-F.	Phase field	2	100	∼30	340	Diffuse interface model that captures 3D physics.	(16, 17)
PF2	D.A.C.	Phase field	2	100	∼50	340	Variational boundary condition sets the contact angle.	(18)
LS1	R.V. M.P.	Level set	2	100	24.9	n.a.	Quasi-static; simulates trapped fluid via immobile "masks."	(19–22)
VF1	J.M. S.G.	Volume-of-fluid	2	100, 60	∼80	340	Implemented in OpenFOAM as an internal VOF solver (interFoam).	(23, 24) (23, 24)
PN1	M.V. A.H.	Pore network	2	100	n.a.	340	Single pressure, dynamic model; ignores the out-of-plane curvature.	(25, 26) (25, 26)
PN2	E.S. R.H.	Pore network	2	100	n.a.	340	Single pressure, dynamic model; ignores the out-of-plane curvature.	(27, 28)
PN3	B.K.P. B.Z. C.W.M. R.J.	Pore network	2	100	n.a.	340	Single pressure, dynamic model; includes the out-of-plane curvature; quasi-static version of the model captures corner flow.	(29, 30)
PN4	Z.Y.	Pore network	2	100	n.a.	340	Single pressure, dynamic model; includes the out-of-plane curvature.	(31)
PN5	C.Y. B.C.	Pore network	2	100	n.a.	n.a.	Quasi-static model for strong drainage; includes the out-of-plane curvature.	(32, 33)

See *SI Appendix*, Notes 3–5 for further details on methods. Dim., dimensionality; Comp. dom., radius of computational domain as a percentage of the radius of the experimental domain; Res., resolution of the computational domain in micrometers per grid block/lattice; n.a., not applicable. LB1, LB2, LB3, LB4, SR1, blue in Fig. 4; PF1, PF2, LS1, VF1, orange in Fig. 4; PN1, PN2, PN3, PN4, PN5, green in Fig. 4.

APPLIED PHYSICAL SCIENCES

Quantitative Performance Measures. For quantitative comparison, we calculate four performance measures from the displacement pattern at the end of each simulation, when the invading fluid reaches the outer edge of the domain:

i) Fractal dimension D_f, as calculated via the box-counting method. This is a classical measure of the degree to which a pattern fills space in 2D (40).

ii) Average dimensionless finger width W_f, as measured at half the radius of the computational domain and scaled by the median post diameter. Note that this measure is very sensitive to domain size for compact displacements and that not all groups used the same domain size.

iii) Gap-averaged saturation S of the invading fluid in invaded regions, as represented by its median value as well as the first and third quartiles. Note that many methods ignore films and therefore assume $S = 1$ in invaded regions.

iv) Displacement efficiency E_d, which is the fraction of the defending fluid that has been displaced from the domain.

Details on how we calculated the quantitative performance measures can be found in *SI Appendix*, Note 2.

Submission of Simulation Results. While some teams submitted results for many of the conditions in the experimental phase diagram (Fig. 1), most teams only contributed results for a relevant subset of the priority cases (Table 1 and *SI Appendix*). For example, some methods were developed for quasi-static displacement (i.e., small Ca) and therefore could not be applied to intermediate or high Ca conditions (LS1, PN5). Other methods were developed for drainage only and therefore could not be applied to imbibition scenarios (PN4, PN5). Additionally, some teams simulated a subset of the experimental domain (i.e., truncated at
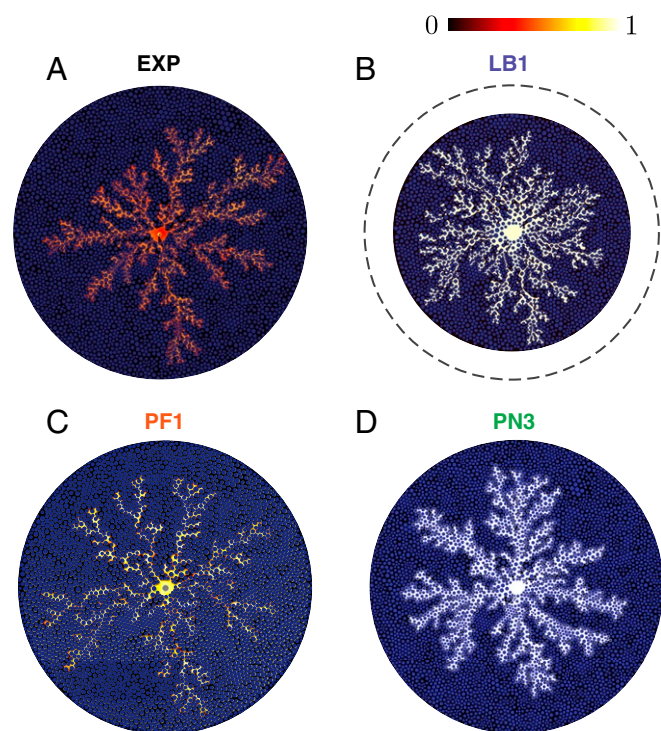

Fig. 3. Selection of simulated displacement patterns for the priority cases. (*A*) Strong drainage at high Ca (SD-HC) as simulated by a phase-field model. (*B*) Weak imbibition at low Ca (WI-LC) as simulated by a pore-network model. (*C*) Strong imbibition at intermediate Ca (SI-IC) as simulated by a lattice Boltzmann model at a reduced viscosity ratio ($\mathcal{M} = 40$). (*D*) Strong imbibition at low Ca (SI-LC) as simulated by a pore-network model.

a smaller outer radius) due to computational constraints (LB1, LB3, SR1, VF1).

Performance of the Methods.

SD-HC. The experimental displacement pattern for SD-HC displays classical viscous fingering, known for the slender, ramified fingers mimicked by diffusion-limited aggregation (Figs. 1 and 2*A*) (41, 42). Remarkably, all three classes of methods are able to capture these patterns (Fig. 2 and *SI Appendix*, Fig. S1). Quantitative analysis of the simulated patterns reveals that while most methods reproduce W_f to within a factor of 60%, most methods overpredict D_f, and all methods overpredict E_d, often by severalfold (Fig. 4*A*). The latter discrepancy is a consequence of incomplete pore-scale displacement due to the well-known formation of thin trailing films of the defending fluid in drainage at high Ca (43, 44). Most methods ignore these films, and those that capture them tend to underpredict their thickness, which corresponds to overpredicting S (Fig. 4*A*). The PF methods appear to do a reasonable job of capturing this incomplete displacement without simulating the full 3D problem. Note that LB1, LB3, SR1, and VF1 simulate a subset of the full domain and that LB1, LB3, and SR1 simulate at a reduced $\mathcal{M}$. Displacement at high Ca is very sensitive to viscosity ratio, and the predictions of the latter methods are affected accordingly.

WI-LC. The experimental displacement pattern for WI-LC shows compact displacement as a result of cooperative pore filling (27, 45). Qualitatively, all three classes of methods are again able to capture these patterns (*SI Appendix*, Fig. S2). Most methods capture D_f to within a few percent, suggesting that the methods reproduce the 2D features of the pattern (Fig. 4*B*). This case does not feature thin films, so S is nearly 1; as a result, those methods that capture D_f also capture E_d. Note that LB1, SR1, and VF1 simulate a subset of the full domain, and LB1 and SR1

Fig. 2. (*A–D*) Comparison between (*A*) the experimental displacement pattern (EXP) and (*B–D*) selected simulated displacement patterns for the case of strong drainage at high Ca (SD-HC). The simulations capture the slender, ramified fingering patterns of SD-HC well, although they are produced by three distinctly different classes of modeling methods. The three methods differ most strongly in how well they reproduce the residual wetting films, as illustrated by the colormap.
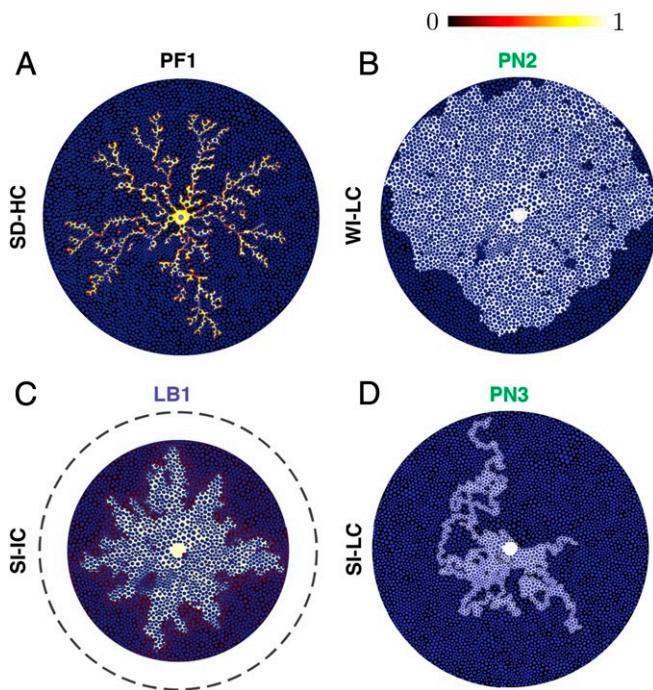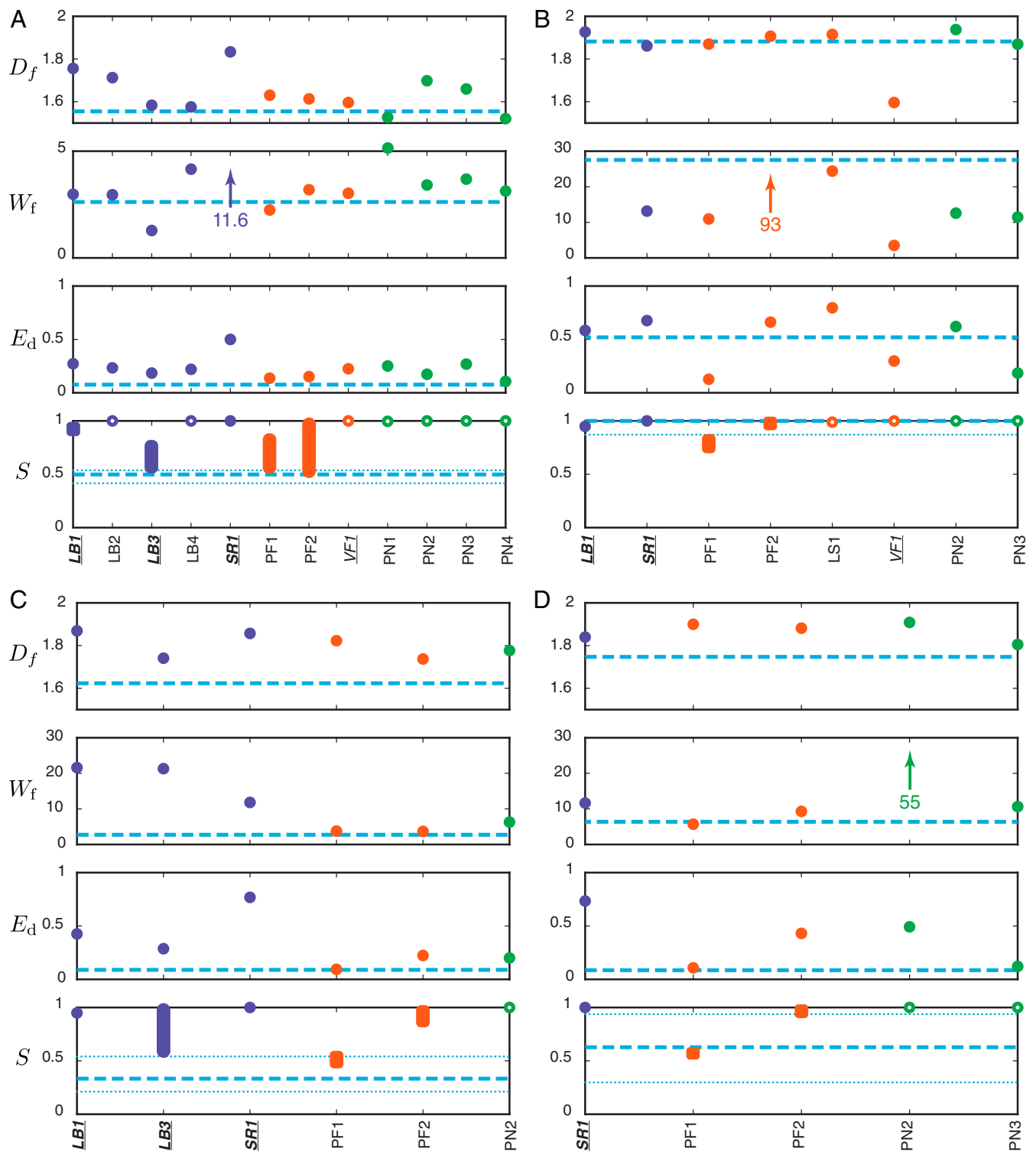
Fig. 4. (A–D) Quantitative performance results for (A) SD-HC, (B) WI-LC, (C) SI-IC, and (D) SI-LC. First row: Fractal dimension D_f. Second row: Average dimensionless finger width W_f. Third row: Displacement efficiency E_d. Fourth row: Gap-averaged saturation S of the invading fluid in invaded regions, with symbols spanning the range from first quartile to third quartile. In the latter, open circles indicate methods that neglect films and therefore assume $S = 1$ in invaded regions. In all cases, we also plot the corresponding experimental measurement (dashed blue line); for S, we show the first and third quartiles (dotted blue lines) in addition to the median value. Italic and underlined labels on the horizontal axis denote contributions that simulate a subset of the experimental domain, while labels in boldface type denote contributions that simulate at a reduced $\mathcal{M}$ relative to the experiments.

simulate at a reduced $\mathcal{M}$. Displacement at low Ca is not very sensitive to viscosity ratio, so the latter two methods still perform well in this scenario.

SI-IC. The experimental displacement pattern for SI-IC shows a highly ramified, yet roughly axisymmetric fingering pattern, the backbone of which is formed by the successive "chaining" of

posts by preferential flow along the postwall corners (2). The resulting pattern has low values of S because the strongly wetting invading fluid propagates primarily by corner flow and in thin films along the top and bottom walls, bypassing pore bodies (2, 46, 47). Qualitatively, none of the methods reproduce the ramified backbone of linked posts (*SI Appendix*, Fig. S3). Most methods fail to capture the emergence of corner flow, typically overestimating W_f and greatly overestimating E_d (Fig. 4C). Fully 3D methods should be able to capture corner flow and film flow, and images from the 3D simulations (LB1, LB3, SR1) suggest that they do, at least to some extent (Fig. 5). However, because of the high computational demands, all three of these methods simulate subsets of the full domain at greatly reduced $\mathcal{M}$; the latter suppresses the strong preferential flow through thin films that should occur for large $\mathcal{M}$. Quasi-3D (gap-averaged) phase-field methods (PF1, PF2) can capture film flow through their upscaled representation of the affinity of the invading fluid for both the walls and the posts, but cannot capture corner flow without an explicit submodel for the presence of corners. Pore-network models would require explicit submodels for both film flow and corner flow.

SI-LC. The experimental displacement pattern for SI-LC is completely controlled by nearly quasi-static invasion through corner flow. Corner films link groups of posts via bursts, and then surrounded pores fill slowly and almost completely. Unlike SI-IC, these patterns have a relatively large value of S and no axial symmetry or well-defined fingers or branches. Relatively few participants attempted this case because it involves both low Ca (computationally demanding for 3D methods) and corner flow (absent from most methods). Qualitatively, the simulation results

are quite variable (*SI Appendix*, Fig. S4). PN3 captures postchaining via corner flow with a dedicated submodel for corner flow, but does not capture the subsequent filling in (Fig. 3); PF1 captures the rough shape, but without clear postchains. Quantitatively, all methods overpredict D_f, but all methods are relatively close to the experimental value (Fig. 4D). All methods except for PF1 also overpredict W_f by a factor of 2 or more. Only PF1 and PF2 are able to make quantitative predictions of S (SR1, PN2, and PN3 assume $S = 1$); PF1 reproduces the experimental value of S very closely, whereas PF2 significantly overpredicts S. PF1 and PN3 both capture E_d relatively well; PF1 is arguably the best match overall.

Thin Films and Corner Flow. The complex nature of interfacial flows in the presence of solid surfaces lends an inherently 3D nature to fluid–fluid displacement processes, even in quasi-1D geometries such as capillary tubes (48) and quasi-2D geometries such as Hele–Shaw cells (46). In a patterned micromodel, these 3D effects include the propagation of thin films along the top and bottom walls and the surfaces of the posts, and in the corners where the walls and posts meet (2, 47). While both fully 3D methods (LB1, LB3) and quasi-3D (gap-averaged) methods (PF1, PF2) predict the formation of trailing films in SD-HC, only fully 3D methods (LB1, LB3) capture films in SI-IC. The color-gradient wetting model used in LB1 leads to an artificial film (~14 µm) that slowly permeates the entire simulation domain. This film accumulates on the posts to form corner films and pendular rings that resemble those observed in the experiments (Fig. 5B). However, this film also uniformly coats the top and bottom walls, and the resulting mass transport appears to suppress the strong preferential flows observed in the experiment. LB3 uses a similar wetting model and should therefore have the same feature (Fig. 5C). Both of these methods are very computationally demanding due to the very large number of particles needed to resolve a 3D flow. For a given scenario, the computational cost also scales with the number of timesteps and the timestep size. The timestep size is constrained by $\mathcal{M}$ for numerical stability, whereas the number of timesteps to breakthrough scales with the domain size. As a result, LB1 and LB3 simulate a subset of the full domain and at a reduced $\mathcal{M}$.

Discussion

The goal of this benchmark study was to assess the degree to which different state-of-the-art modeling strategies could reproduce the correct macroscopic features (and some pore-scale features) of fluid–fluid displacement in a porous medium under different wetting conditions. These pore-scale models have become widely used tools in extracting macroscopic properties of geologic porous media (e.g., relative permeability) (49–52) and in designing synthetic porous materials with desirable transport properties for use in electrochemical devices (53, 54). In all of these cases, the accuracy of the model output hinges upon its ability to correctly account for the impact of wettability at different capillary numbers.

Most methods were able to capture viscous instability and fingering at high flow rates (IC and HC), and most were also able to capture the more subtle broadening of features in WI where the low contact angle enables cooperative pore filling. In contrast, few methods were able to capture the thin trailing films that form for SD-HC, the thin leading films that occur for SI-IC, and the corner films that dominate SI-LC, all of which are inherently 3D.

For 2D models, films present a modeling challenge. Gap-averaged PF models were able to capture trailing films in SD-HC, although leading films in SI-IC and corner flow in SI-LC remain elusive. Other 2D models were unable to capture films to any noteworthy extent. PN3 was the only model to explicitly account for corner flow and was reasonably successful in doing so for quasi-static displacement. However, extending such
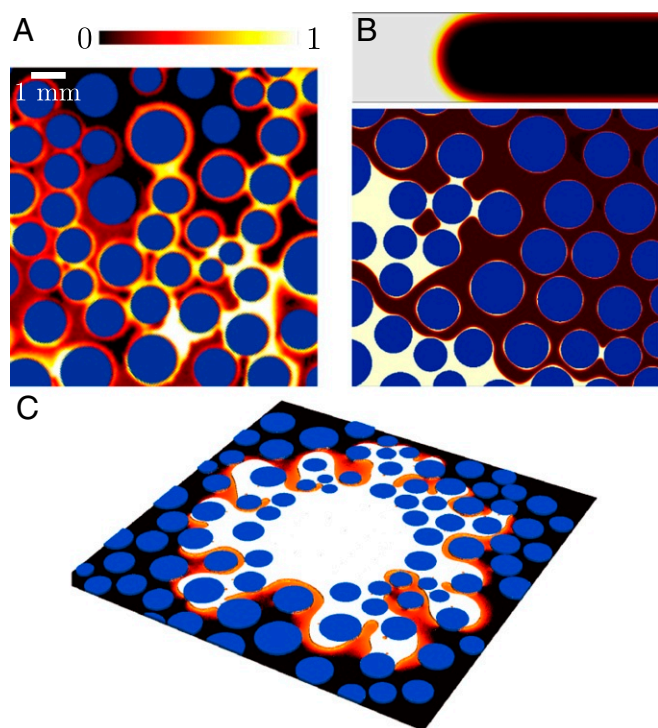

Fig. 5. (*A*) Experimental snapshot of SI-IC at the pore scale, which is characterized by the coexistence of thin films and corner flow. (*B*) Simulation results of LB1 for SI-IC ($\mathcal{M} = 40$). (*B*, *Top*) Cross-sectional view showing the leading thin films along the top and bottom walls. (*B*, *Bottom*) Plan view showing the coexistence of thin films and corner flow, as well as pendular rings that link neighboring posts. (*C*) Isometric projection of the 3D simulation results of LB3 for SI-IC ($\mathcal{M} = 100$), showing the propagation of thin films ahead of the main invasion front.

a model to include viscous effects and residual films is nontrivial because many of the underlying physical phenomena, such as flow through corner networks, film bridging from post to post, and postchaining avalanches, are poorly understood.

For 3D models, films present a serious computational challenge. Resolving films is nontrivial due to the large aspect ratio of the problem—the radius of the flow cell is 100 mm, the gap thickness is 100 μm, and the film thickness ranges from tens of micrometers to a few micrometers or less. LB1, LB2, and LB3 addressed this challenge most directly, running 3D simulations with ∼160 million, ∼160 million, and ∼300 million lattice sites, respectively. Even after reducing the viscosity ratio and truncating the domain to relax timestep restrictions, these simulations required world-class computational resources. Despite this substantial effort, these simulations could achieve a spatial resolution of only 10–20 μm, which is barely small enough to allow for films and certainly not small enough to resolve them. All three groups agree that this problem pushes the limits of what is currently possible. More importantly, these simulations showed both qualitatively and quantitatively that failure to resolve films at the small scale can have important consequences for the macroscopic flow pattern.

It is well known that preexisting wetting films are common in subsurface applications such as enhanced oil recovery and that their presence has a significant impact on the macroscopic transport properties such as relative permeability (55, 56). These preexisting films would be an active, evolving component of the displacement as they swell, disconnect, reconnect, and pinch off—particularly in partial wetting conditions. Resolving them (and the flow within them) would be an essential and challenging part of the problem.

This benchmark targets the "many-pore" scale (hundreds to thousands of pores), as this is a scale large enough to manifest the collective dynamics characteristic of fluid–fluid displacements in porous media (viscous fingering, capillary fingering, avalanches, etc.) and small enough that computational models are routinely used to make predictions. Thus, it is natural to ask whether those predictions are accurate. There is, however, an underlying scale at which "single-pore" mechanisms emerge (such as meniscus deformation and merging, contact-line pinning and motion, contact-angle hysteresis, post wetting dynamics, etc.). The inclusion of these effects will further increase the computational complexity of the problem, which makes it impractical at the scale of hundreds to thousands of pores considered in the current study. The comparison of different methods at this single-pore scale would require an altogether different type of benchmark study in a simpler geometry (e.g., Verma *et al.* (21)).

Furthermore, real rocks such as carbonates also have a wider pore-size distribution than the one from our micromodel (57), a feature that would likely have an effect on the correlation between pore occupancy and pore size that is absent from our experimental benchmark.

A key contribution of this benchmark is to demonstrate the capabilities and limitations of three major classes of pore-scale models (i.e., lattice/particle-based models, continuum models, and pore-network models) in predicting the macroscopic features of unstable two-phase flows in the presence of solid surfaces. We find that all three classes of models are capable of predicting the transition from strong drainage to weak imbibition. Specifically, pore-network models offer superior computational efficiency, but they lack the ability to resolve gap-averaged saturations that the more computationally intensive lattice/particle-based models and continuum models offer. Only 3D lattice/particle-based models could simulate leading films and corner flow in strong imbibition, but their spatial and temporal resolutions are severely limited by computational demand. Our results highlight the need for further effort along multiple complementary avenues in what is already a very active area of research.

Materials and Methods

The simulated displacement patterns for all priority cases are presented in *SI Appendix*, Figs. S1–S4. Details on how we calculated the quantitative performance measures of the priority cases can be found in *SI Appendix*, Note 2. Descriptions of all of the models, including their derivation and numerical implementation, are included in *SI Appendix*, Notes 3–5.

1. M. J. Blunt *et al.*, Pore-scale imaging and modelling. *Adv. Water Resour.* **51**, 197–216 (2013).
2. B. Zhao, C. W. MacMinn, R. Juanes, Wettability control on multiphase flow in patterned microfluidics. *Proc. Natl. Acad. Sci. U.S.A.* **113**, 10251–10256 (2016).
3. J. P. Stokes *et al.*, Interfacial stability of immiscible displacement in a porous medium. *Phys. Rev. Lett.* **57**, 1718–1721 (1986).
4. M. Trojer, M. L. Szulczewski, R. Juanes, Stabilizing fluid-fluid displacements in porous media through wettability alteration. *Phys. Rev. Appl.* **3**, 054008 (2015).
5. J. M. Al-Besharah, O. A. Salman, S. A. Akashah, Viscosity of crude oil blends. *Ind. Eng. Chem. Res.* **26**, 2445–2449 (1987).
6. Y. Chen, Y. Li, A. J. Valocchi, K. T. Christensen, Lattice Boltzmann simulations of liquid CO_2 displacing water in a 2D heterogeneous micromodel at reservoir pressure conditions. *J. Contam. Hydrol.* **212**, 14–27 (2018).
7. J. Zhao *et al.*, Simulation of microscale gas flow in heterogeneous porous media based on the lattice Boltzmann method. *J. Appl. Phys.* **120**, 084306 (2016).
8. H. Liu, A. J. Valocchi, Q. Kang, Three-dimensional lattice Boltzmann model for immiscible two-phase flow simulations. *Phys. Rev. E* **85**, 046309 (2012).
9. H. Liu, A. J. Valocchi, C. Werth, Q. Kang, M. Oostrom, Pore-scale simulation of liquid CO_2 displacement of water using a two-phase lattice Boltzmann model. *Adv. Water Resour.* **73**, 144–158 (2014).
10. J. E. McClure, J. F. Prins, C. T. Miller, A novel heterogeneous algorithm to simulate multiphase flow in porous media on multicore CPU-GUP systems. *Comput. Phys. Commun.* **185**, 1865–1874 (2014).
11. J. E. McClure, M. A. Berrill, W. G. Gray, C. T. Miller, Tracking interface and common curve dynamics for two-fluid-phase flow in porous media. *J. Fluid Mech.* **796**, 211–232 (2016).
12. A. Fakhari, D. Bolster, Diffuse interface modeling of three-phase contact line dynamics on curved boundaries: A lattice Boltzmann model for large density and viscosity ratios. *J. Comput. Phys.* **334**, 620–638 (2017).
13. A. Fakhari, Y. Li, D. Bolster, K. T. Christensen, A phase-field lattice Boltzmann model for simulating multiphase flows in porous media: Application and comparison to experiments of CO_2 sequestration at pore scale. *Adv. Water Resour.* **114**, 119–134 (2018).
14. T. Hiller, M. S. De La Lama, M. Brinkmann, Stochastic rotation dynamics of wetting multi-phase flows. *J. Comput. Phys.* **315**, 554–576 (2016).
15. M. Jung *et al.*, Wettability controls slow immiscible displacement through local interface instabilities. *Phys. Rev. Fluids* **1**, 074202 (2016).
16. L. Cueto-Felgueroso, R. Juanes, A phase-field model of two-phase Hele-Shaw flow. *J. Fluid Mech.* **758**, 522–552 (2014).
17. L. Cueto-Felgueroso, R. Juanes, Macroscopic phase-field model of partial wetting: Bubbles in a capillary tube. *Phys. Rev. Lett.* **108**, 144502 (2012).
18. D. A. Cogswell, M. L. Szulczewski, Simulation of incompressible two-phase flow in porous media with large timesteps. *J. Comput. Phys.* **345**, 856–865 (2017).
19. M. Prodanović, S. L. Bryant, A level set method for determining critical curvatures for drainage and imbibition. *J. Colloid Interf. Sci.* **304**, 442–458 (2006).

APPLIED PHYSICAL SCIENCES

20. E. Jettestuen, J. O. Helland, M. Prodanović, A level set method for simulating capillary-controlled displacements at the pore scale with nonzero contact angles. *Water Resour. Res.* **49**, 4645–4661 (2013).

21. R. Verma, M. Icardi, M. Prodanović, Effect of wettability on two-phase quasi-static displacement: Validation of two pore scale modeling approaches. *J. Contam. Hydrol.* **212**, 115–133 (2018).

22. R. Verma, "Pore scale modeling of multiphase flow in heterogeneously wet media," PhD thesis, The University of Texas at Austin, Austin, TX (2018).

23. S. Pavuluri, J. Maes, F. Doster, Spontaneous imbibition in a microchannel: Analytical solution and assessment of volume of fluid formulations. *Microfluidic Nanofluidic* **22**, 90 (2018).

24. J. Maes, S. Geiger, Direct pore-scale reactive transport modelling of dynamic wettability changes induced by surface complexation. *Adv. Water Resour.* **111**, 6–19 (2018).

25. E. Aker, K. J. Måløy, A. Hansen, G. G. Batrouni, A two-dimensional network simulator for two-phase flow in porous media. *Transp. Porous Med.* **32**, 163–186 (1998).

26. H. A. Knudsen, E. Aker, A. Hansen, Bulk flow regimes and fractional flow in 2D porous media by numerical simulations. *Transp. Porous Med.* **47**, 99–121 (2002).

27. R. Holtzman, E. Segre, Wettability stabilizes fluid invasion into porous media via nonlocal, cooperative pore filling. *Phys. Rev. Lett.* **115**, 164501 (2015).

28. R. Holtzman, Effects of pore-scale disorder on fluid displacement in partially-wettable porous media. *Sci. Rep.* **6**, 36221 (2016).

29. B. K. Primkulov et al., Quasi-static fluid-fluid displacement in porous media: Invasion-percolation through a wetting transition. *Phys. Rev. Fluids* **3**, 104001 (2018).

30. B. K. Primkulov et al., Signatures of fluid-fluid displacement in porous media: Wettability, patterns, and pressures. arXiv:1906.02364 (6 June 2019).

31. Z. Yang, A. Niemi, F. Fagerlund, T. Illangasekare, Two-phase flow in rough-walled fractures: Comparison of continuum and invasion-percolation models. *Water Resour. Res.* **49**, 993–1002 (2013).

32. C. Yuan, B. Chareyre, F. Darve, Pore-scale simulations of drainage in granular materials: Finite size effects and the representative elementary volume. *Adv. Water Resour.* **97**, 109–124 (2016).

33. C. Yuan, B. Chareyre, A pore-scale method for hydromechanical coupling in deformable granular media. *Comput. Methods Appl. Mech. Eng.* **318**, 1066–1079 (2017).

34. S. Chen, G. D. Doolen, Lattice Boltzmann method for fluid flows. *Annu. Rev. Fluid Mech.* **30**, 329–364 (1998).

35. T. Ihle, D. M. Kroll, Stochastic rotation dynamics: A Galilean-invariant mesoscopic model for fluid flow. *Phys. Rev. E* **63**, 020201 (2001).

36. C. W. Hirt, B. D. Nichols, Volume of fluid (VOF) method for the dynamics of free boundaries. *J. Comput. Phys.* **39**, 201–225 (1981).

37. J. A. Sethian, P. Smereka, Level set methods for fluid interfaces. *Annu. Rev. Fluid Mech.* **35**, 341–372 (2003).

38. V. E. Badalassi, H. D. Ceniceros, S. Banerjee, Computation of multiphase systems with phase field models. *J. Comput. Phys.* **190**, 371–397 (2003).

39. M. J. Blunt, Flow in porous media—pore-network models and multiphase flow. *Curr. Opin. Colloid Interf. Sci.* **6**, 197–207 (2001).

40. M. R. Schroeder, *Fractals, Chaos, Power Laws: Minutes From an Infinite Paradise* (W. H. Freeman and Company, Dover ed., 2009).

41. L. Paterson, Diffusion-limited aggregation and two-fluid displacements in porous media. *Phys. Rev. Lett.* **52**, 1621–1624 (1984).

42. K. J. Måløy, J. Feder, T. Jøssang, Viscous fingering fractals in porous media. *Phys. Rev. Lett.* **55**, 2688–2691 (1985).

43. G. I. Taylor, Deposition of a viscous fluid on the wall of a tube. *J. Fluid Mech.* **10**, 161–165 (1961).

44. F. P. Bretherton, The motion of long bubbles in tubes. *J. Fluid Mech.* **10**, 166–188 (1961).

45. M. Cieplak, M. O. Robbins, Influence of contact angle on quasistatic fluid invasion of porous media. *Phys. Rev. B*, **41**, 11508–11521 (1990).

46. B. Levaché, D. Bartolo, Revisiting the Saffman-Taylor experiment: Imbibition patterns and liquid-entrainment transitions. *Phys. Rev. Lett.* **113**, 044501 (2014).

47. C. Odier, B. Levaché, E. Santanach-Carreras, D. Bartolo, Forced imbibition in porous media: A fourfold scenario. *Phys. Rev. Lett.* **119**, 208005 (2017).

48. B. Zhao, A. A. Pahlavan, L. Cueto-Felgueroso, R. Juanes, Forced wetting transition and bubble pinch-off in a capillary tube. *Phys. Rev. Lett.* **120**, 084501 (2018).

49. P. C. Reeves, M. A. Celia, A functional relationship between capillary pressure, saturation, and interfacial area as revealed by a pore-scale network model. *Water Resour. Res.* **32**, 2345–2358 (1996).

50. H. Rajaram, L. A. Ferrand, M. A. Celia, Prediction of relative permeabilities for unconsolidated soils using pore-scale network models. *Water Resour. Res.* **33**, 43–52 (1997).

51. P. H. Valvatne, M. J. Blunt, Predictive pore-scale modeling of two-phase flow in mixed wet media. *Water Resour. Res.* **40**, W07406 (2004).

52. L. Hao, P. Cheng, Pore-scale simulations on relative permeabilities of porous media by lattice Boltzmann method. *Int. J. Heat Mass Transf.* **53**, 1908–1913 (2010).

53. P. P. Mukherjee, Q. Kang, C. Y. Wang, Pore-scale modeling of two-phase transport in polymer electrolyte fuel cells – progress and perspective. *Energy Environ. Sci.* **4**, 346–369 (2011).

54. F. Arbabi, H. Montazeri, R. Abouatallah, R. Wang, A. Bazylak, Three dimensional computational fluid dynamics modelling of oxygen bubble transport in polymer electrolyte membrane electrolyzer porous transport layers. *J. Electrochem. Soc.* **163**, F3062–F3069 (2016).

55. M. Blunt, M. J. King, H. Scher, Simulation and theory of two-phase flow in porous media. *Phys. Rev. A* **46**, 7680–7699 (1992).

56. M.-H. Hui, M. Blunt, Effects of wettability on three-phase flow in porous media. *J. Phys. Chem. B* **104**, 3833–3845 (2000).

57. M. J. Blunt, *Multiphase Flow in Permeable Media: A Pore-Scale Perspective* (Cambridge University Press, 2017).